Journal Pre-proof

Strong yet strain-hardenable equiatomic CoCrFeMnNi high-entropy alloys by dynamic heterostructuring

Jungwan Lee, Hyojin Park, Sujung Son, Takayoshi Nakano, Hyoung Seop Kim

This is a PDF file of an article that has undergone enhancements after acceptance, such as the addition of a cover page and metadata, and formatting for readability, but it is not yet the definitive version of record. This version will undergo additional copyediting, typesetting and review before it is published in its final form, but we are providing this version to give early visibility of the article. Please note that, during the production process, errors may be discovered which could affect the content, and all legal disclaimers that apply to the journal pertain.

© 2023 Published by Elsevier.

Strong yet strain-hardenable equiatomic CoCrFeMnNi high-entropy alloys by dynamic heterostructuring

Jungwan Lee[a], Hyojin Park[a], Sujung Son[a], Takayoshi Nakano[b], Hyoung Seop Kim[a,c,d,e,f,*]

[a] *Department of Materials Science and Engineering, Pohang University of Science and Technology (POSTECH), Pohang, 37673, Republic of Korea*

[b] *Division of Materials and Manufacturing Science, Graduate School of Engineering, Osaka University, 2-1 Yamadaoka, Suita, Osaka 565-0871, Japan*

[c] *Graduate Institute of Ferrous & Energy Materials Technology (GIFT), Pohang University of Science and Technology (POSTECH), Pohang, 37673, Republic of Korea*

[d] *Center for Heterogenic Metal Additive Manufacturing, Pohang University of Science and Technology (POSTECH), Pohang, 37673, Republic of Korea*

[e] *Institute for Convergence Research and Education in Advanced Technology, Yonsei University, Seoul 03722, South Korea*

[f] *Advanced Institute for Materials Research (WPI-AIMR), Tohoku University, Sendai, 980-8577, Japan*

*Corresponding author: Hyoung Seop Kim,

E-mail address: hskim@postech.ac.kr Tel: +82-54-279-2150

ABSTRACT

Heterostructuring gives solutions to achieve better mechanical performance of metallic materials. For instance, partial static recrystallization by short-term annealing induces bimodal grain size distribution. Distinct from the well-studied 'static heterostructuring' by cold rolling followed by annealing, this study introduces 'dynamic heterostructuring' by hot rolling. Dynamic recrystallization (DRX) during the hot rolling as a softening mechanism leaves room for dislocation accumulation. With the expectations of enhanced strain hardening of the as-rolled materials with the aid of the DRX, we monitored tensile responses of the as-hot-rolled equiatomic CoCrFeMnNi high-entropy alloys (HEAs). Among the hot rolling temperatures from 800 °C to 900 °C with a thickness reduction ratio of 78.6% for the HEAs, the hot rolling at 850 °C results in a bimodal grain size distribution, i.e., partial DRX. It comprises relatively fine DRXed grains and coarse unrecrystallized grains: the latter is harder than the DRXed ones with relatively low dislocation density. The microstructural heterogeneity results in uniform elongation of ~13% due to the accumulation of dislocations at the grain boundaries inside the soft DRXed grains. This endows the as-hot-rolled single-phase HEAs with strain hardenability without the aid of phase transformation, deformation twinning, or precipitates. In addition, the hot-rolled HEAs with high dislocation density have doubled yield stresses of those of conventionally cold-rolled and annealed counterparts. Considering the industrial benefits of the simplified thermo-mechanical control processes, this work extends the academic and practical value of DRX by dynamic heterostructuring through annealing-free hot-rolling.

Keywords: A. metals and alloys; C. grain boundaries, mechanical properties, microstructure, D. scanning electron microscopy, SEM

1. Introduction

Beefing up mechanical properties lies at the heart of concerns for metallurgists to ensure the soundness of advanced structural materials in a variety of extreme environments. In particular, high yield stress as well as decent formability is essential for automotive, aerospace, and energy industries with their increasingly high standards for safety [1,2]. Recently, a number of heterostructuring strategies have provided appreciable pathways to achieve better mechanical performance. For instance, metal additive manufacturing is a new-fangled metallurgical field that efficiently renders microstructural heterogeneity with cellular structures by its thermal effects [3,4]. On the other hand, phase decomposition and recrystallization kinetics have been specifically governed to cope with the heterostructural design for the wrought metallic materials [5–7]. For instance, partial recrystallization is a salient key to promoting strain hardening due to microstructural incompatibility between hard unrecrystallized and soft recrystallized grains [6–9]. This scenario originates from the short-term annealing of severe plastic deformed alloys at certain temperatures. However, in a practical view, a mishandling of annealing time by just a few tens of seconds can dramatically change the recrystallization fraction and the size of recrystallized grains [10]. That is, the mechanical responses can be degraded once the optimum annealing condition is not reached. In addition, plastic deformation followed by annealing takes significant time and costs. Thus, more feasible and concise thermo-mechanical control processes are required for the successful deployment of the advanced materials and processes linked to desirable mechanical responses in commercial products.

In the alloy design landscape, high-entropy alloys (HEAs) have emerged as a new alloying concept due to their versatile characteristics including mechanical [11–13],

anticorrosive [14,15], and magnetic properties [16,17]. For the mechanical responses, single face-centered-cubic (FCC) HEAs involving Co, Cr, Ni, and other metallic or even organic elements exhibit noticeable strain hardening [12,18,19]. However, a low yield stress is a major drawback of the FCC HEAs. In terms of upgrading the yield stress, cold-rolled HEAs with high dislocation density give superior yield stress, but a lack of strain hardenability makes them impractical to be used as sought-after structural materials [20,21].

Meanwhile, various metallic materials experience dynamic recrystallization (DRX) under hot plastic deformation [22–28]. The DRXed fraction, texture, and grain size of the equiatomic CoCrFeMnNi HEAs have been carefully examined by controlling the temperature and strain rate of the hot compression/rolling [27]. However, to the best of our knowledge, the effect of the DRXed microstructures induced by the hot rolling on the mechanical responses of HEAs has hardly been discussed in detail. In this regard, we monitored the tensile properties of as-hot-rolled HEAs in relation to the DRX behavior with the expectations that the DRX, especially partial DRX for dynamic heterostructuring, could introduce strain hardenability for the as-hot-rolled HEAs. The dynamic heterostructuring by hot rolling is distinguished from conventional 'static heterostructuring' by cold rolling and heat treatment involving partial static recrystallization.

To determine the sole effect of the DRX-induced dynamic heterostructuring on strain hardening without any aid of transformation-induced plasticity (TRIP) or precipitation, which has been a hot topic toward the record-breaking combinations of strength and ductility for the past few years [29,30], a single-phase CoCrFeMnNi HEA was considered as the target alloy. By hot rolling at several temperatures that result in different DRX behaviors, partially DRXed microstructures were obtained at certain rolling temperatures. Thanks to the dynamic

4

heterogeneity of grain sizes of the as-hot-rolled HEAs, strain hardening occurred with uniform elongation of 13% during the tensile deformation at an ambient temperature despite the absence of annealing. The dynamic heterostructuring offers a solution for the notoriously low uniform elongation of the as-rolled HEAs. Thus, this study can greatly raise their industrial applications while retaining the benefits of the high-yield stress compared to the annealed ones.

2. Experimental

Four equiatomic CoCrFeMnNi HEA ingots were cast using vacuum induction melting (MC100V, Indutherm, Germany) under an argon atmosphere with elements of 99.99% purity. The ingots were homogenized at 1100 ℃ under the argon atmosphere for 6 hours followed by water quenching. The homogenized ingots of a 7-mm thickness were hot-rolled at 800, 825, 850, and 900 ℃ down to a thickness of 1.5 mm by a 78.6% thickness reduction ratio, followed by air quenching. The thickness reduction ratio per each rolling pass was 15%. After every two back-and-forth rolling passes, the rolled plate was reheated in a furnace for 5 minutes to retain the hot rolling temperature and to avoid redundant grain growth [31]. The hot-rolled specimens are referred to as HR800, HR825, HR850, and HR900 according to the hot-rolling temperatures in degree Celsius. Given that full recrystallization occurs by annealing at 800 ℃ for an hour after cold rolling with the same thickness reduction for the same alloy [32], the four hot rolling temperatures were anticipated to provoke the DRX.

Dog-bone-shaped tensile specimens of gauge length 5 mm, width 2.5 mm, and thickness 1.5 mm, were obtained along the rolling direction (RD) of the hot-rolled plates. The tensile specimens were polished using SiC papers up to 1200-grit to remove oxides on both surface layers. The specimens were white- and black-sprayed for the accurate measurement of

elongation and local strain distribution during the tensile deformation using digital image correlation (DIC). Tensile tests at an ambient temperature with a nominal strain rate of 10^{-3} s^{-1} were conducted using universal testing equipment (Instron 5582, Instron Corp., USA), accompanying the DIC with ARAMIS 12M (GOM, Germany) installation. Each mechanical test was conducted three times for data reproducibility.

Microstructures of the as-hot-rolled and tensile deformed samples were analyzed using electron backscatter diffraction (EBSD) and electron channeling contrast imaging (ECCI) with a field emission scanning electron microscope (FE-SEM, JSM-7900F). The EBSD analyses utilized an Oxford AZtec*HKL* system. The samples were polished with SiC papers up to 1200-grit on the transverse directional (TD) plane, beneficial to observe nano-scale dislocation structures of the as-hot-rolled plates [33]. Electrochemical polishing was exploited on a mechanically polished surface using a solution of 92% acetic acid + 8% perchloric acid at 28 V for 25 seconds, which shows the best image quality. The EBSD step size was 0.7 μm for images at low magnification of 180×. The EBSD step sizes of more magnified images are presented in the figure captions. For the ECCI, an electron beam intensity of 20 kV, a probe current of 18 μA, a working distance of 5.5 mm, and a tilting degree from –2° to 2° were applied using a backscattered electron detector of the FE-SEM. X-ray diffraction (XRD) analysis was performed on the hot-rolled HEAs using a Bruker D8 Advance diffractometer with Cu K$_\alpha$ radiation under a range of diffraction angle (2θ) from 30° to 100° and each step size was 0.013°.

3. Results

3.1. As-hot-rolled microstructures

3.1.1. Identifying DRX grains

Figure 1 gives inverse pole figure (IPF) maps of the hot-rolled HR800 with a minority of fine DRXed grains. Generally, annealing-induced partially recrystallized grains can be identified by a grain orientation spread (GOS) criterion of 2° [33,34]. In contrast, for the as-hot-rolled cases, DRXed grains are exposed to hot rolling deformation after nucleation until the hot rolling is finalized; plenty of the DRXed grains have GOS values above 2°. Thus, a higher GOS criterion than 2° is required as reported in other partially recrystallized microstructures by hot rolling [23]. In the present HEA, the grains with GOS values below 6° obviously reveal the fine DRXed grains of the HR800 in Fig. 1(b), whose areal fraction is 16.6%. Using the GOS criterion of 2° in Fig. 1(d), lots of the DRXed grains are misidentified as unrecrystallized grains, compared to Fig. 1(c) with the criterion of 6°. Hereafter, the recrystallized/unrecrystallized grains are referred to as 'DRX/NonDRX grains.' The grain size distribution in Fig. 1(f) excluding twin boundaries shows that a large portion belongs to the NonDRX grains. The average grain size of the NonDRX grains of ~400 μm in Fig. 1(h) is larger than that of the as-homogenized state of ~136 μm before the hot rolling in Supplementary Fig. S1(a), while that of the DRX grains is 6.65 ± 7.64 μm. Note that a clear dark grain of an ECC image in Supplementary Fig. S1(b) indicates a lack of dislocations before the hot rolling. It infers that dislocations generated during the hot rolling promote the migration of grain boundaries and coarsen the NonDRX grains. The dislocation structures of the as-hot-rolled states using the ECCI are given in the latter part.
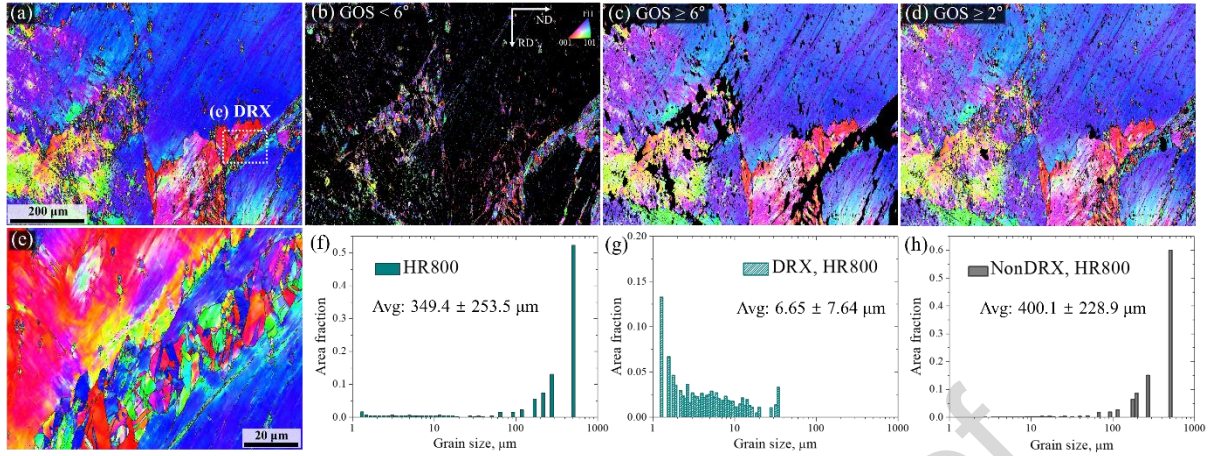
7

Figure 1. (a–e) EBSD IPF maps of the hot-rolled microstructures of the HR800. Grains with GOS values (b) below 6°, (c) above 6°, and (d) above 2°. (e) An enlarged view of DRX grains in (a) with an EBSD step size of 90 nm. (f–h) Grain size distributions of the HR800 for the (f) whole, (g) DRX, and (h) NonDRX grains. RD and ND in (b) mean rolling and normal directions, respectively.

Meanwhile, the DRX grains mostly exist along the grain boundaries of the coarse NonDRX grains as shown in Fig. 1(a and e). The necklace structure of the fine DRX structure is the typical morphology of the DRXed microstructures [22,23,28]. Given the low areal fraction of the DRX, the DRX grains are presumed to be newly recrystallized. In Fig. 1(e), the newly generated DRX grains exhibit random orientations regardless of those of the adjacent NonDRX grains. Because of the insufficient number of the DRX grains, the texture analysis is not made in the HR800.

3.1.2. Texture of DRX grains and grain size distribution

An increase in hot rolling temperature accelerates the driving force of the DRX [28,34].

8

Moreover, the grain growth of the DRX is also dependent on the hot rolling temperature because the migration of the grain boundaries is a thermally activated process. The grain growth rate (v) follows an Arrhenius-type equation [35]:

$$v = v_0 \exp\left(-\frac{Q_0}{RT}\right), \tag{1}$$

where v_0 is a preexponential constant and Q_0 is the activation energy for the grain boundary migration. R and T are the gas constant and temperature, respectively. Thus, the increase in hot rolling temperature awakens both the DRX and the grain growth.

To figure out the DRX grains in the HR825 in Fig. 2(a), the same GOS criterion of 6° was used in Fig. 2(b and c). The DRX fraction of the HR825 is appreciably increased to 64.8% compared to that of the HR800. In a yellow dotted box in Fig. 2(b), some DRX grains are located inside a NonDRX grain, which are assumed to originate from the shear bands of the NonDRX grain. Considering that stored energy by rolling deformation is locally concentrated in the shear bands, the shear bands can serve as the nucleation sites of the DRX as well as grain boundaries [24]. Note that the IPF map colors of the DRX grains at the shear bands in the NonDRX grain in the yellow box are different from those of the other DRX grains in the red box in Fig. 2(b). For the texture analysis of the numerous fine DRX grains, orientation distribution function (ODF) maps of $\varphi_2 = 0°$ and 45° sections of the DRX grains are plotted in Fig. 2(d–f). Overall, {011}//ND α-fiber and {111}//ND γ-fiber are prominent in the DRX grains in Fig. 2(d), which are typical rolling textures of FCC metallic materials [36]. A large portion of the DRX grains in the red box in Fig. 2(b) exhibits {011}<100> Goss, which belongs to the α-fiber in Fig. 2(e). In contrast, the α-fiber is not detected in the DRX grains at the shear bands in Fig. 2(f), which corresponds to the yellow box in Fig. 2(b). Instead, these DRX grains display the γ-fiber. In general, γ-fiber has higher stored energy than α-fiber [37]. It concurs

9

with the high stored energy of the shear bands where the rolling deformation is locally concentrated. Indeed, the DRX grains nucleated at the shear bands are exposed to a larger amount of rolling deformation than the other DRX grains.
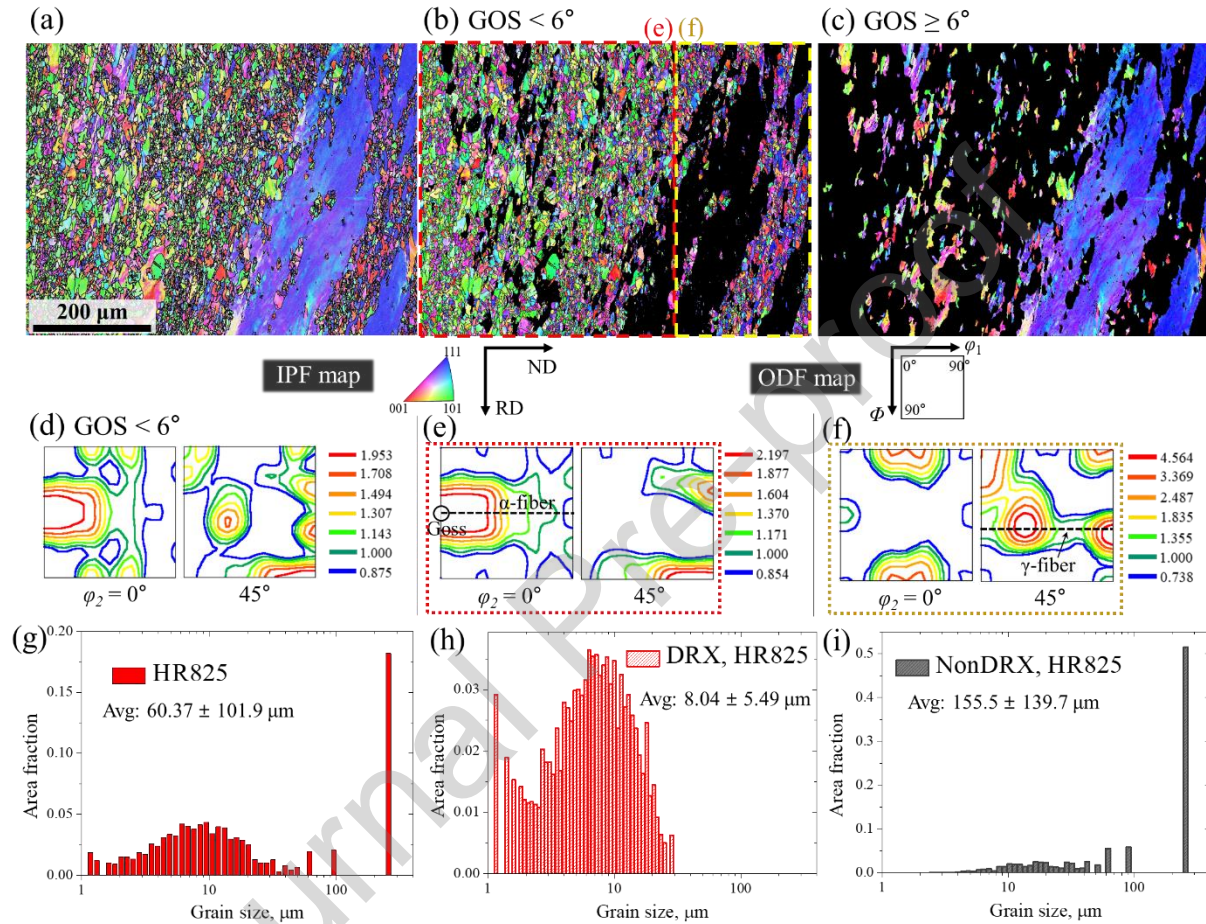

Figure 2. Hot-rolled microstructures of the HR825. EBSD IPF maps of (a) the entire area, (b) DRX, and (c) NonDRX grains with a GOS criterion of 6°. (d) ODF φ_2 = 0° and 45° sections of the DRX grains in (b). (e, f) ODF sections of the separate parts in the red and yellow dotted boxes in (b), respectively. (g–i) Grain size distributions of the HR825 for the (g) whole, (h) DRX, and (i) NonDRX grains.

As well as the areal fraction, an average grain size of 8.04 ± 5.49 μm of the DRX grains

of the HR825 in Fig. 2(h) is higher than that of the HR800 because of the more active DRX and grain growth with an increase in hot rolling temperature. Due to the increased fraction of the DRX grains, the average grain size of the NonDRX grains in Fig. 2(i) decreases in the HR825. However, the entire grain size distribution in Fig. 2(g) still shows a large discrepancy in areal fraction of each grain between the DRX and NonDRX grains, making it hard to call a balanced bimodal grain size distribution. To boost the effect of the microstructural heterogeneity between the DRX and NonDRX grains, the vast grain sizes of the NonDRX grains need to be decreased by the increase in the DRX fraction.

With a further increase in the hot rolling temperature, the HR850 shows the balanced grain size distribution between the DRX and NonDRX grains in Fig. 3 due to the more vigorous DRX behavior. In the EBSD IPF maps of the HR850 in Fig. 3(a–c), the same GOS criterion distinguishes the DRX grains. The sites of the DRX – grain boundaries or shear bands – are hard to be identified in Fig. 3(b) due to the active DRX behavior with an areal fraction of 73.7%. The average grain size of 8.27 ± 5.93 μm of the DRX grains in the HR850 in Fig. 3(e) is slightly higher than that of the HR825 in Fig. 2(h). In contrast, the average NonDRX grain size of several tens of micrometers in the HR850 in Fig. 3(f) is markedly reduced by the increase in the DRX fraction, rendering the bimodal grain size distribution in Fig. 3(d).

Meanwhile, the texture of the DRX grains of the HR850 exhibits γ-fiber without any trace of α-fiber in Fig. 3(g). It indicates that the DRX grains have been exposed to more rolling deformation compared to the HR825. As hot rolling temperature increases, DRX becomes more prevalent; the DRX occurs in earlier rolling passes, and more amount of deformation is applied to the DRX grains until the final thickness is reached. In this regard, the texture analyses in Figs. 1–3 exhibit the evolution of the main texture of the DRX grains according to the increase

11

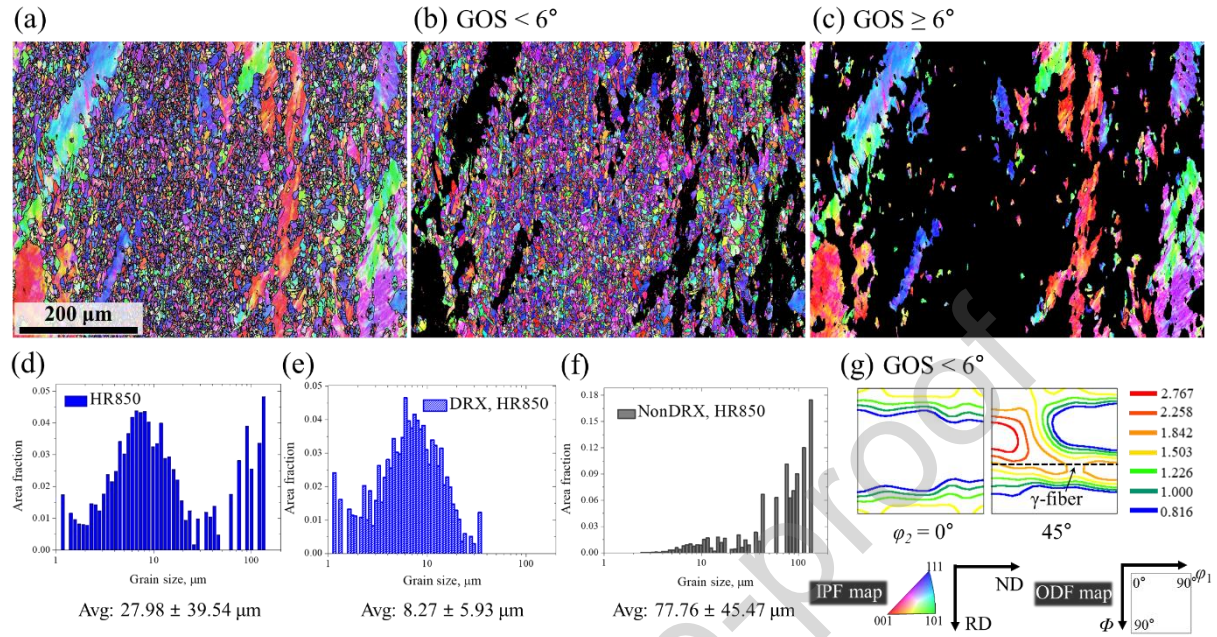in the hot rolling temperature: random orientations → α-fiber → γ-fiber.

Figure 3. Hot-rolled microstructures of the HR850. EBSD IPF maps of (a) the entire area, (b) DRX, and (c) NonDRX grains. (d–f) Grain size distributions of the HR850 for the (d) whole, (e) DRX, and (f) NonDRX grains. (g) ODF φ_2 = 0° and 45° sections of the DRX grains in (b).

3.1.3. DRX fraction according to hot rolling temperature

For the HR900, all the hot-rolled grains are DRXed with several annealing twins, see Fig. 4(a). The DRX grains mainly exhibit γ-fiber in Fig. 4(b) as in the case of the HR850. The average grain size is 9.16 ± 5.27 μm in Fig. 4(c), a bit coarser than that of the DRX grains of the HR850 due to the active grain growth at high rolling temperature. The DRX fractions of the four as-hot-rolled microstructures according to the hot rolling temperature are illustrated in Fig. 4(d). For the identification of constituent phases, the XRD profiles of the four hot-rolled

12

HEAs in Supplementary Fig. S2 exhibit a single FCC phase without any precipitates. As such, the hot rolling temperature range from 800 °C to 900 °C is suitable to render the different areal fractions of the DRX grains in the single-phase hot-rolled HEAs.
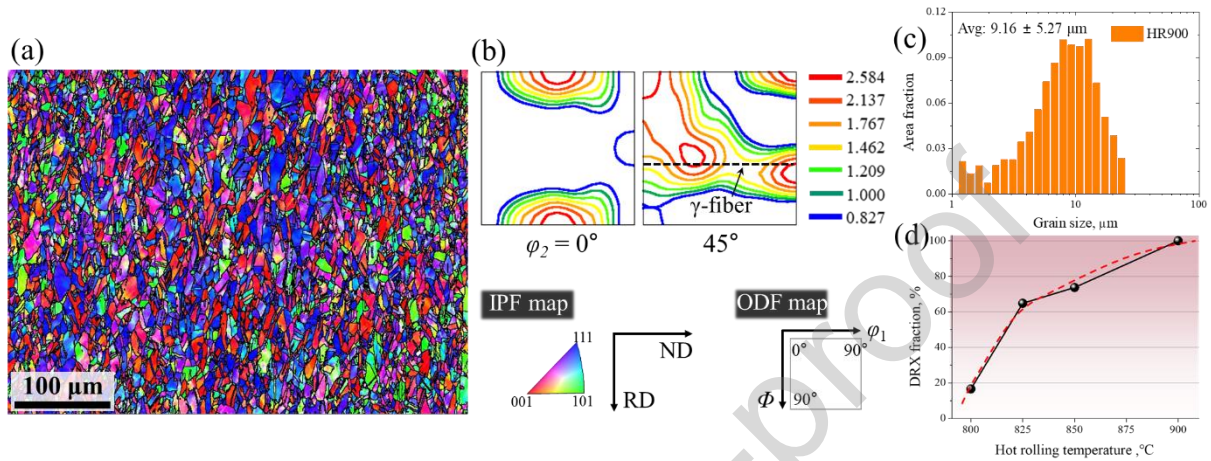

Figure 4. EBSD (a) IPF map, (b) ODF $\varphi_2 = 0°$ and 45° sections, and (c) grain size distribution of the HR900. (d) The DRX fractions of the as-hot-rolled HEAs according to the hot rolling temperature.

3.2. Mechanical properties

Tensile properties at an ambient temperature of the as-hot-rolled CoCrFeMnNi HEAs are exhibited in Fig. 5(a–c) and Table 1. Yield stress of 770.3 ± 6.5 MPa of the HR800 with the least DRX fraction is the highest among the four cases. The yield stress decreases as the hot rolling temperature increases in Fig. 5(a and b). Nonetheless, the HR825 and HR850 have doubled yield stresses of those of the fully recrystallized ones by annealing after cold rolling which exhibit similar total elongation in Fig. 5(d) [10,21,32,38–43]. Even when compared to the cases of partially recrystallized ones by annealing, the HR825 and HR850 exhibit better combinations of yield strength and total elongation.
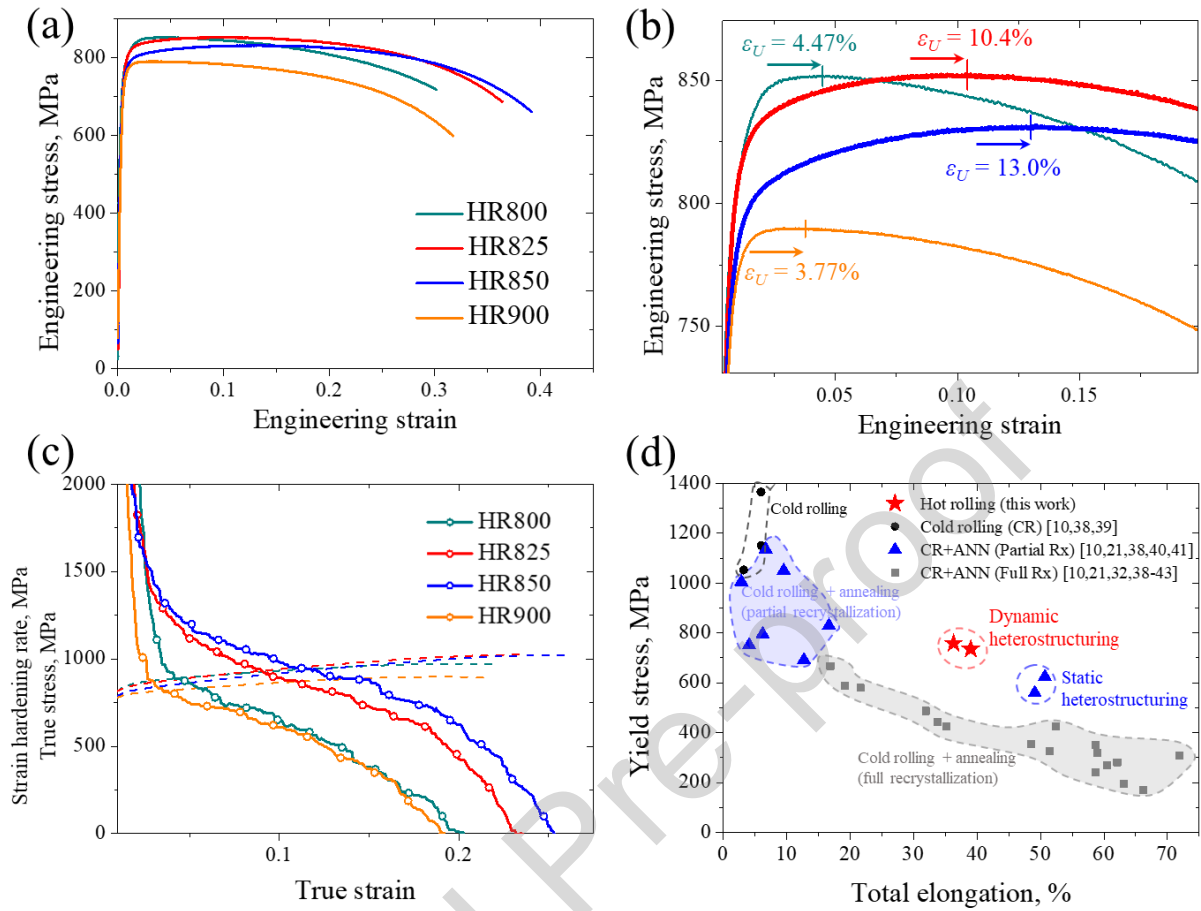
13

Figure 5. Tensile properties at an ambient temperature of the as-hot-rolled CoCrFeMnNi HEAs. (a, b) Engineering stress-strain curves and (c) strain hardening rate curves plotted with the true stress-strain curves. (d) Combinations of yield stress and total elongation of the HR825 and HR850 (dynamic heterostructuring) with a variety of processing routes of the present HEAs: cold rolling [10,38,39], annealing for partial recrystallization, i.e., static heterostructuring [10,21,38,40,41], and annealing for full recrystallization [10,21,32,38–43]. The notation "CR+ANN" indicates cold rolling followed by annealing.

Table 1. Tensile properties at an ambient temperature of the four as-hot-rolled CoCrFeMnNi HEAs. YS, UTS, U. El., and T. El. stand for yield stress, ultimate tensile stress, uniform

elongation, and total elongation, respectively.

	YS, MPa	UTS, MPa	UTS − YS, MPa	U. El., %	T. El., %
HR800	770.3 ± 6.5	853.0 ± 8.8	82.7	4.47 ± 0.47	29.0 ± 1.6
HR825	758.4 ± 1.7	848.6 ± 3.8	90.2	10.4 ± 1.03	36.3 ± 2.6
HR850	735.4 ± 3.4	830.7 ± 0.9	95.3	13.0 ± 0.33	39.0 ± 1.4
HR900	718.8 ± 3.8	797.9 ± 6.3	81.1	3.77 ± 0.34	31.9 ± 0.7

The HR800 shows a poor uniform elongation of 4.47 ± 0.47% in Fig. 5(b), which is a typical drawback of conventional as-rolled metallic materials. On the contrary, the HR825 and HR850 indicate doubled and tripled uniform elongation of 10.4 ± 1.03% and 13.0 ± 0.33%, respectively, compared to that of the HR800. Notably, the uniform and total elongation of the HR850 in Table 1 are remarkable regarding the as-rolled state. In stark contrast, the fully DRXed HR900 with the lowest yield stress exhibits a meager uniform elongation of 3.77 ± 0.34%, similar to that of the HR800. Accordingly, only the HR825 and HR850 are strain-hardenable as shown in the strain hardening rate curves in Fig. 5(c). The two curves of the HR825 and HR850 are clearly above the other two during the tensile deformation. Given the marginal DRX in the HR800 and the full DRX in the HR900, the bimodal distribution of grain sizes due to the coexistence of the DRX and NonDRX grains in the HR825 and HR850 seems to unleash the strain hardening behavior. Not only the grain sizes, but the internal dislocation densities of the DRX and NonDRX grains will differ because the DRX is a softening mechanism by alleviating the dislocation density. In other words, compared to the DRX grains, the NonDRX grains seem to have higher dislocation density; they would be relatively hard.

15

Once the tensile deformation is applied to the heterogeneous microstructures, dislocations tend to accumulate at the grain boundaries inside the soft grains because strain incompatibility rises across the soft/hard domain boundary [8,9]. In this regard, monitoring the changes in geometrically necessary dislocation (GND) densities of the DRX and NonDRX grains is essential to figure out the microstructural heterogeneity conducive to the hetero-deformation-induced strain hardening.

3.3. Tensile deformation in heterostructured HEAs by partial DRX

To figure out the origin of strain hardening of the HR850 exhibiting the most balanced bimodal microstructure and the highest uniform elongation, the microstructural evolution by the tensile deformation needs to be probed. Before the tensile deformation, Fig. 6(a) gives an ECC image of the as-hot-rolled HR850 presenting both plenty of DRX grains and a relatively coarse NonDRX grain elongated along the RD. Several annealing twins indicate that their matrices belong to the DRX. The grain boundary between the DRX and NonDRX grains is magnified in Fig. 6(b) with a different ECC tilt angle of 2° toward the best contrast image. The clearly dark DRX grain indicates a minority of dislocations and no microbands inside. On the other hand, the NonDRX grain consists of multiple microbands elongated along the RD with a submicron-scale thickness, providing a sharp contrast image within the grain. Given that the microbands originate from in-grain shear zones bounded by the GNDs [44], the GNDs induced by local rotation to accommodate the orientation misfits during the hot rolling give rise to the boundary conditions in the NonDRX grain, *viz.*, forming the microbands [45]. The comparison of the GND density between the DRX and NonDRX grains is made in the following paragraph. As well as the GNDs, the relatively coarse grain size of the NonDRX grain also contributes to

16

forming the microbands compared to the fine DRX grains because a decrease in grain size inhibits the generation of the microbands [44].
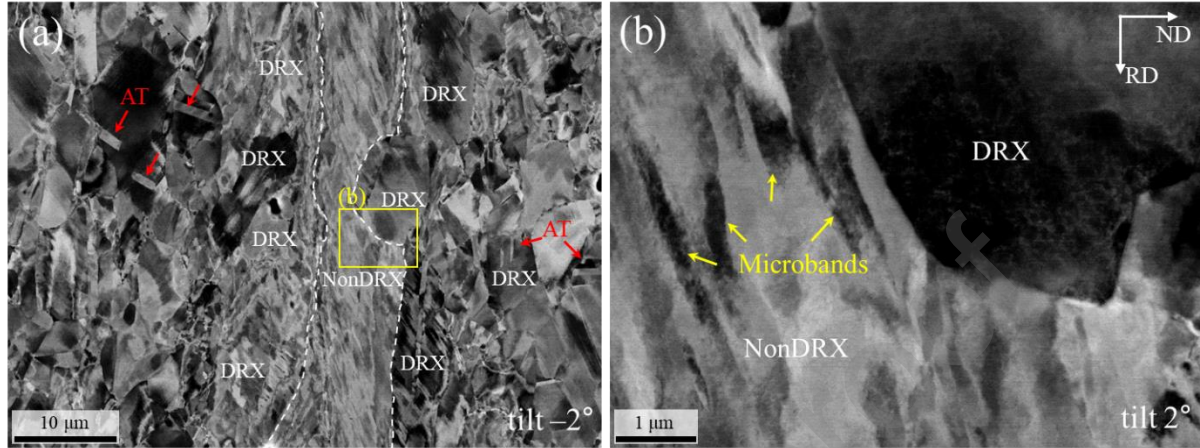

Figure 6. ECC images of the as-hot-rolled HR850 with a tilt angle of (a) –2° and (b) 2°, where (b) is an enlarged part of a yellow box in (a). Red arrows in (a) and yellow arrows in (b) represent annealing twins and microbands, respectively.

For the microstructural evolution upon a tensile strain, EBSD IPF and GND density maps of the initial and tensile deformed HR850 by a true strain (ε) of 0.1 are given in Fig. 7(a–f). The local true strain is tracked by DIC images, indicated in Fig. 7(g and h). For the HR850, ε of 0.1 is right before necking of ε of 0.122 in Fig. 5(c). The NonDRX grains of the initial state of the HR850 have higher GND density than the DRX grains as shown in EBSD GND density maps in Fig. 7(b and c). It accords with the lack of dislocations in the DRX grain as shown in the ECCI in Fig. 6(b). The difference in the dislocation density is attributed to the more rolling deformation in the NonDRX grain, given the hot rolling-induced microbands in the NonDRX grain in Fig. 6(b). Comparably speaking, the NonDRX grain is harder than the DRX grain. According to the misorientation profiles in the DRX and NonDRX grains in Fig. 7(i and j)

17

along the red and black arrows in Fig. 7(a), respectively, no noticeable misorientation is observed in the single DRX grain but profuse misorientation peaks of ~2° exist in the NonDRX grain. Note that the misorientation angles in the NonDRX grain conform to those of the microbands of 1.0° ~ 2.5° in austenitic steel [46]. Thus, the numerous low-angle misorientations in the NonDRX grain support the widely distributed microbands; some of them are confirmed in Fig. 6(b).
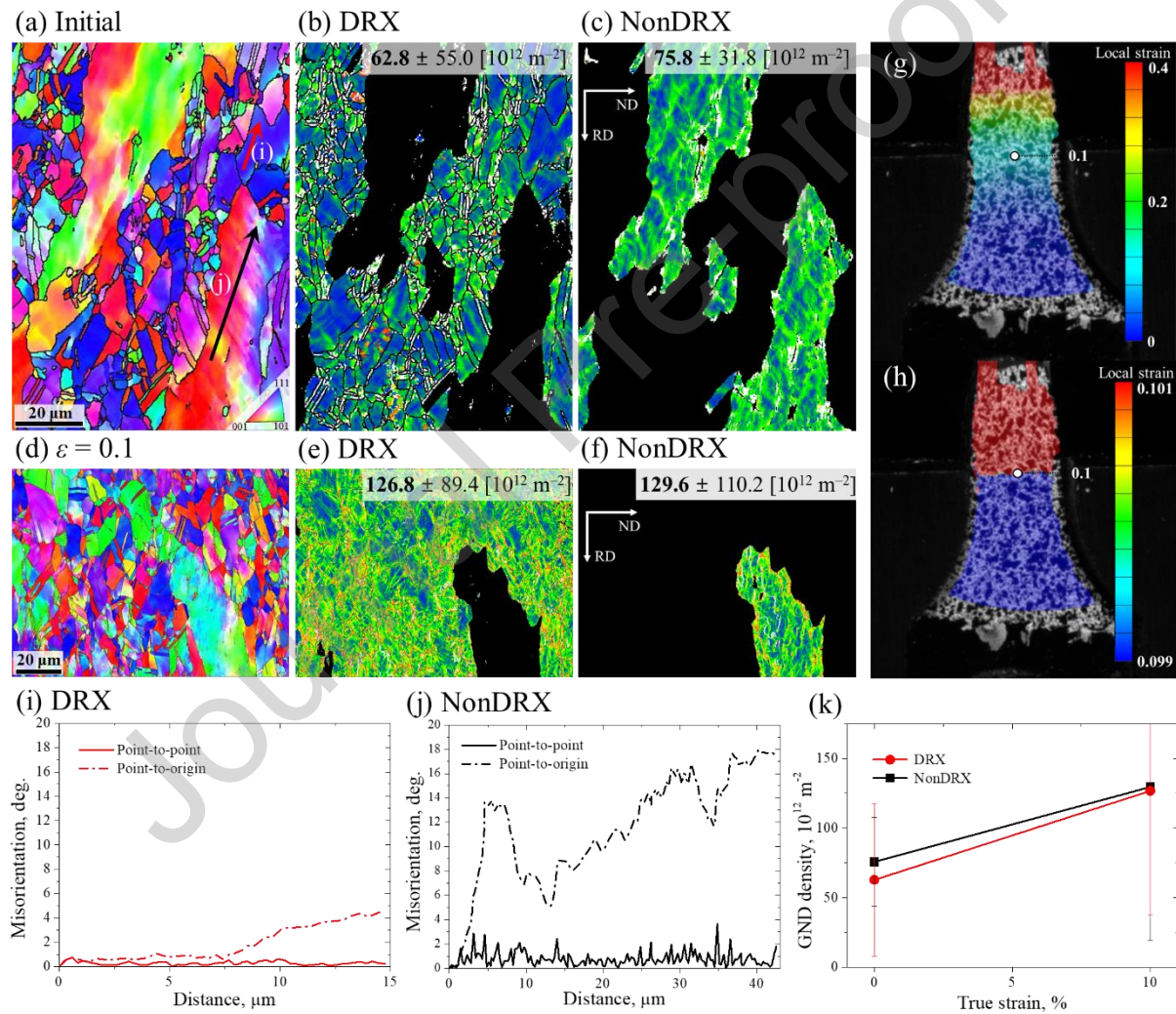

Figure 7. EBSD (a, d) IPF maps and GND density maps for the (b, e) DRX and (c, f) NonDRX grains of the (a–c) initial and (d–f) tensile deformed HR850 by a true strain (ε) of 0.1. (g) A local strain map for the fractured HR850 obtained by the DIC method. (h) The exact location

corresponding to the ε of 0.1 is shown by a narrower strain range. (i, j) One-dimensional misorientation profiles of a single DRX and NonDRX grains along the red and black arrows in (a), respectively. (k) demystifies the GND density evolution of the DRX and NonDRX grains upon the true strain. The EBSD step size for each map is 80 nm.

As tensile deformation is applied, an increase in the GND density of the DRX grains is higher than that of the NonDRX grains in Fig. 7(e, f, and k). It infers that more dislocations are accumulated in the DRX grains because of the strain incompatibility between the relatively soft DRX and the hard NonDRX grains. This awakens back stress in the HR850. Moreover, the back stress induced by the GNDs in the soft DRX grains alleviates resolved shear stress for the dislocation slip; the DRX grains accommodate enhanced plastic strain due to the promoted dislocation slip [47]. Meanwhile, no deformation-induced phase transformation occurs during the tensile deformation in Supplementary Fig. S3. In brief, the dislocation accumulation in the soft DRX grains results in the strain hardening without the aid of TRIP or twinning effect despite the as-hot-rolled states. Considering that the fully DRXed HR900 exhibits the poor uniform elongation in Fig. 5(b), the coexistence of the DRX and NonDRX grains is essential for the strain hardenability.

4. Discussion

4.1. Dislocation accumulation in wavy slip in DRX

For the direct confirmation of the dislocation accumulation between the DRX and NonDRX grains, Fig. 8 gives ECC images of the HR850 deformed by ε of 0.1 in the uniform

deformation stage. A relatively coarse NonDRX grain elongated along the RD and several DRX grains coexist in Fig. 8(a). In an enlarged view in Fig. 8(b), regarding the mottled appearance of the DRX grain in the ECC image, the DRX grain has orientation gradients containing microbands. It is in stark contrast to the clear dark image of a DRX grain of the initial state in Fig. 6(b), implying that the tensile deformation has developed the local orientation gradients and dislocations in the DRX grains. According to a more magnified view in Fig. 8(c), prevalent dislocation cells corresponding to wavy slip are generated in the DRX grain near the grain boundary during the deformation. In contrast, with a different ECC tilt angle which gives a dark contrast in the NonDRX grain in Fig. 8(d), much fewer dislocations are amassed at the grain boundary into the NonDRX side. Thus, the ECC images in Fig. 8(c and d) directly show that dislocations are accumulated at the grain boundaries into the relatively soft DRX grain, coincident with the GND density evolution in Fig. 7. In other words, it can be safely argued that the orientation gradient and the microbands in the DRX grains arise from the accumulation of the dislocations during the tensile deformation. The tangled dislocations in the wavy slip in the DRX grains can provoke dislocation hardening, thus carry more uniform elongation [48]. Considering the large fraction of 73.7% of the DRX grains in Fig. 3(b), the generation of dislocations in the DRX grains is beneficial to the strain hardening of the HR850.
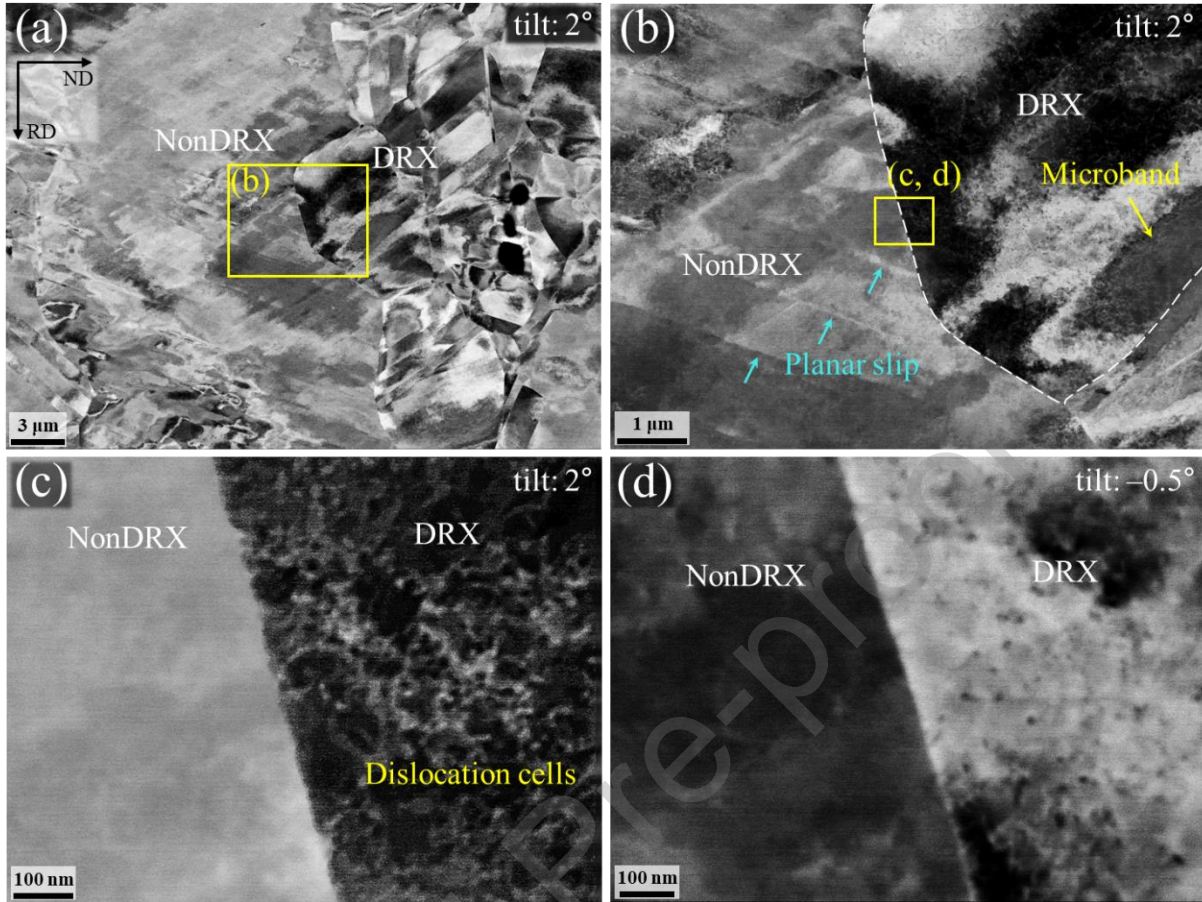
Figure 8. ECC images of the tensile deformed HR850 by a true strain of 0.1. (a) shows several DRX grains and a NonDRX grain elongated along the RD. (b) is an enlarged part of (a). (c, d) exhibit an enlarged part of (b) with different ECC tilt angles: (c) 2° and (d) –0.5°.

In contrast to the dislocation cells in the DRX grain in Fig. 8(c), planar slip lines are observed in the NonDRX grain in Fig. 8(b). The planar and wavy slip can emerge in the CoCrFeMnNi HEAs by differing grain sizes [49]. In large grains, a single slip system is awakened during the tensile deformation [50]. At an ambient temperature, stacking fault energy (SFE) of the equiatomic CoCrFeMnNi HEA is $18.3 \sim 27.3$ mJ/m^2 [51]. The low SFE and the single slip system lead to planar slip in the NonDRX grain. On the other hand, multiple slip

systems can be activated in small grains at the same deformation level because of limited conditions of strain compatibility with regard to the surrounding small grains [49,50]. The operation of the multiple slip systems gives rise to an increase in cross-slip probability and wavy slip. Moreover, in spite of the low SFE, the DRX as a softening mechanism involving dynamic recovery during the hot rolling promotes cross-slip; the planarity of dislocation slip is relaxed [24,50]. Thus, the formation of the dislocation cell structures in wavy slip in the DRX grain in Fig. 8(c) is attributed to the relatively small grain size and the DRX mechanism. Regarding the absence of dislocation barriers except for grain boundaries and the seamless transition from planar to wavy slip in the DRX grain, the accumulation of dislocations in the DRX grain is the main contributor to the strain hardening of the hot-rolled HEAs.

4.2. Effect of hot rolling on improving yield stress

The doubled yield stress of the HR850 compared to those of the fully recrystallized ones by annealing in Fig. 5(d) is considered to originate from high dislocation density of the HR850. It can be extrapolated by a prominently higher kernel average misorientation value of the as-hot-rolled HR850 than that of the annealed one [32] in Supplementary Fig. S4. The effect of hot-rolled textures on yield stress can be neglected regarding their low intensity in Figs. 2(d), 3(g), and 4(b), which is a common feature of FCC metallic materials with low SFE [52,53].

Indeed, the dynamic heterostructuring by the proper adjustment of the hot rolling temperature gives rise to the strong yet fracture-resistant HEAs: the relatively soft DRX grains mainly contribute to strain hardening with appreciable yield stresses. Compared to the marginal uniform elongation of the previously reported as-rolled CoCrFeMnNi HEAs [10,38,39], the present study significantly improves the strain hardening as shown in Fig. 9(a and b). For the

22

partially DRXed microstructures, the balanced bimodal grain size distribution between the DRX and NonDRX groups in the HR850 further enhances the strain hardenability in Fig. 9(c). The point to address is that the grain boundaries between the DRX and NonDRX grains play a key role in accommodating dislocations during the tensile deformation. Given that DRX is commonly observed in hot working processes, it is believed that the dynamic heterostructuring can be applied to other metallic materials beyond the multi-principal element alloying concept.
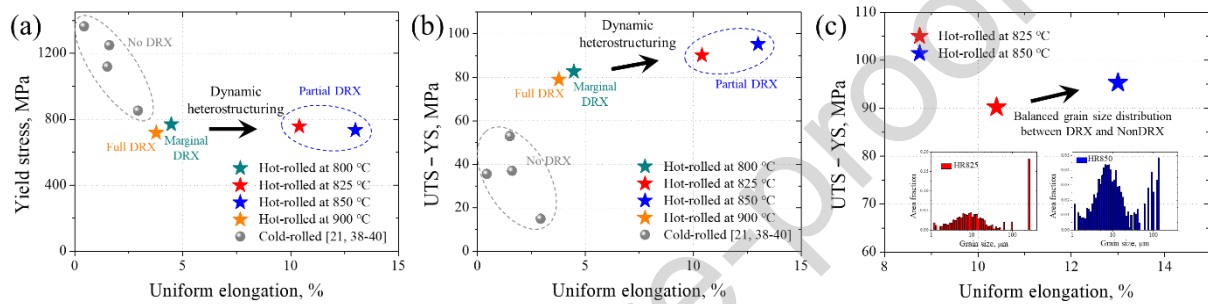

Figure 9. Tensile properties of the as-rolled equiatomic CoCrFeMnNi HEAs comprising hot rolling and cold rolling [10,38,39] with the same thickness reduction: (a) yield stress and uniform elongation and (b) a difference between ultimate tensile stress (UTS) and yield stress (YS) and uniform elongation. (c) An enlarged part of (b) focusing on the HR825 and HR850. The insets in (c) show the grain size distributions of the HR825 and HR850.

5. Conclusion

This study introduces dynamic heterostructuring by a single-step hot rolling for the single-phase equiatomic CoCrFeMnNi HEAs. Despite the as-rolled states without the aid of phase transformation or precipitates, the present study reveals strain hardenability as well as doubled yield stress compared to the conventionally cold-rolled and annealed ones. The major findings are demonstrated below.

23

(1) A proper control of the hot rolling temperature conduces to partially DRXed hot-rolled microstructures with appropriate areal fractions. For the HEAs hot-rolled at 850 °C, a balanced bimodal distribution of grain sizes between the DRX and NonDRX grains is obtained. As well as the grain size heterogeneity, the DRX grains have lower internal dislocation density than the NonDRX grains because the DRX is a softening process by consuming dislocations.

(2) The strain incompatibility between the DRX and NonDRX grains during tensile deformation originates from their different grain characteristics. The dislocation accumulation in wavy slip at the grain boundaries into the relatively soft DRX grains leads to strain hardenability of the HR850 with a uniform elongation of ~13% despite the as-rolled states. Moreover, the dislocations generated by the hot rolling also result in a doubled yield stress of the HR850 compared to those of the cold-rolled and annealed HEAs.

Acknowledgments

References

[1] E. Bayraktar, N. Isac, G. Arnold, An experimental study on the forming parameters of deep-drawable steel sheets in automotive industry, *J. Mater. Proc. Tech.* **162–163** (2005) 471–476. https://doi.org/10.1016/j.jmatprotec.2005.02.059.

[2] S.-Y. Lee, H.-S. Park, J.-H. Kim, F. Barlat, K.-H. Chung, Investigation of elastic modulus

degradation and recovery with time and baking process for deformed automotive steel sheets, *Met. Mater. Int.* **29** (2023) 892–907. https://doi.org/10.1007/s12540-022-01268-8.

[3] E. Maleki, S. Bagherifard, M. Bandini, M. Guagliano, Surface post-treatments for metal additive manufacturing: Progress, challenges, and opportunities, *Addit. Manuf.* **37** (2021) 101619. https://doi.org/10.1016/j.addma.2020.101619.

[4] L. Yang, O. Harrysson, D. Cormier, H. West, H. Gong, B. Stucker, Additive manufacturing of metal cellular structures: design and fabrication, *JOM* **67** (2015) 608–615. https://doi.org/10.1007/s11837-015-1322-y.

[5] Q. Wu, F. He, J. Li, H. S. Kim, Z. Wang, J. Wang, Phase-selective recrystallization makes eutectic high-entropy alloys ultra-ductile, *Nat. Commun.* **13** (2022) 4697. https://doi.org/10.1038/s41467-022-32444-4.

[6] Y. Wang, Y. Zhu, Z. Yu, J. Zhao, Y. Wei, Hetero-zone boundary affected region: A primary microstructural factor controlling extra work hardening in heterostructure, *Acta Mater.* **241** (2022) 118395. https://doi.org/10.1016/j.actamat.2022.118395.

[7] J.-L. Zhang, C. C. Tasan, M. J. Lai, D. Yan, D. Raabe, Partial recrystallization of gum metal to achieve enhanced strength and ductility, *Acta Mater.* **135** (2017) 400–410. https://doi.org/10.1016/j.actamat.2017.06.051.

[8] X. Wu, M. Yang, F. Yuan, Y. Zhu, Heterogeneous lamella structure unites ultrafine-grain strength with coarse-grain ductility, *PNAS* **112** (2015) 47, 14501–14505. https://doi.org/10.1073/pnas.1517193112.

[9] O. Bouaziz, H. S. Kim, J. Lee, Y. Estrin, Bauschinger effect or kinematic hardening: bridging microstructure and continuum mechanics, *Met. Mater. Int.* **29** (2023) 280–292. https://doi.org/10.1007/s12540-022-01227-3.

[10] W. Chen, N. Li, F. Wang, J. Gu, J. He, M. Song, On the dual-stage partial recrystallization and the corresponding mechanical response of the Cantor alloy, *J. Alloys Compd.* **918** (2022) 165651. https://doi.org/10.1016/j.jallcom.2022.165651.

[11] J.-W. Yeh, S.-K. Chen, S.-J. Lin, J.-Y. Gan, T.-S. Chin, T.-T. Shun, C.-H. Tsau, S.-Y. Chang, Nanostructured high-entropy alloys with multiple principal elements: novel alloy design

concepts and outcomes, *Adv. Eng. Mater.* **6** (2004) 5, 299–303. https://doi.org/10.1002/adem.200300567.

[12] B. Gludovatz, A. Hohenwarter, D. Catoor, E. H. Chang, E. P. George, R. O. Ritchie, A fracture-resistant high-entropy alloy for cryogenic applications, *Science* **345** (2014) 6201, 1153–1158. https://doi.org/10.1126/science.1254581.

[13] Y. A. Alshataif, S. Sivasankaran, F. A. Al-Mufadi, A. S. Alaboodi, H. R. Ammar, Manufacturing methods, microstructural and mechanical properties evolutions of high-entropy alloys: a review, *Met. Mater. Int.* **26** (2020) 1099–1133. https://doi.org/10.1007/s12540-019-00565-z.

[14] H. Luo, Z. Li, A. M. Mingers, D. Raabe, Corrosion behavior of an equiatomic CoCrFeMnNi high-entropy alloy compared with 304 stainless steel in sulfuric acid solution, *Corro. Sci.* **134** (2018) 131–139. https://doi.org/10.1016/j.corsci.2018.02.031.

[15] Y. Shi, B. Yang, P. K. Liaw, Corrosion-resistant high-entropy alloys: A Review, *Metals* **7** (2017) 2, 43. https://doi.org/10.3390/met7020043.

[16] V. Chaudhary, R. Chaudhary, R. Banerjee, R. V. Ramanujan, Accelerated and conventional development of magnetic high entropy alloys, *Mater. Today* **49** (2021) 231–252. https://doi.org/10.1016/j.mattod.2021.03.018.

[17] O. Schneeweiss, M. Friák, M. Dudová, D. Holec, M. Šob, D. Kriegner, V. Holý, P. Beran, E. P. George, J. Neugebauer, A. Dlouhý, Magnetic properties of the CrMnFeCoNi high-entropy alloy, *Phys. Rev. B* **96** (2017) 014437. https://doi.org/10.1103/PhysRevB.96.014437.

[18] G. Laplanche, A. Kostka, C. Reinhart, J. Hunfeld, G. Eggeler, E. P. George, Reasons for the superior mechanical properties of medium-entropy CrCoNi compared to high-entropy CrMnFeCoNi, *Acta Mater.* **128** (2017) 292–303. https://doi.org/10.1016/j.actamat.2017.02.036.

[19] Z. J. Gu, Y. Z. Tian, W. Xu, S. Lu, X. L. Shang, J. W. Wang, G. W. Qin, Optimizing transformation-induced plasticity in CoCrNi alloys by combined grain refinement and chemical tuning, *Scr. Mater.* **214** (2022) 114658. https://doi.org/10.1016/j.scriptamat.2022.114658.

[20] J. Gu, M. Song, Annealing-induced abnormal hardening in a cold rolled CrMnFeCoNi

high entropy alloy, *Scr. Mater.* **162** (2019) 345–349. https://doi.org/10.1016/j.scriptamat.2018.11.042.

[21] J. W. Bae, J. Moon, M. J. Jang, D. Yim, D. Kim, S. Lee, H. S. Kim, Trade-off between tensile property and formability by partial recrystallization of CrMnFeCoNi high-entropy alloy, *Mater. Sci. Eng. A* **703** (2017) 324–330. http://dx.doi.org/10.1016/j.msea.2017.07.079.

[22] K. Huang, R. E. Logé, A review of dynamic recrystallization phenomena in metallic materials, *Mater. Des.* **111** (2016) 548–574. http://dx.doi.org/10.1016/j.matdes.2016.09.012.

[23] A. Hadadzadeh, F. Mokdad, M. A. Wells, D. L. Chen, A new grain orientation spread approach to analyze the dynamic recrystallization behavior of a cast-homogenized Mg-Zn-Zr alloy using electron backscattered diffraction, *Mater. Sci. Eng. A* **709** (2018) 285–289. http://dx.doi.org/10.1016/j.msea.2017.10.062.

[24] L. Choisez, L. Ding, M. Marteleur, A. Kashiwar, H. Idrissi, P. J. Jacques, Shear banding-activated dynamic recrystallization and phase transformation during quasi-static loading of β-metastable Ti –12 wt % Mo alloy, *Acta Mater.* **235** (2022) 118088. https://doi.org/10.1016/j.actamat.2022.118088.

[25] X.-Q. Yin, C.-H. Park, Y.-F. Li, W.-J. Ye, Y.-T. Zuo, S.-W. Lee, J.-T. Yeom, X.-J. Mi, Mechanism of continuous dynamic recrystallization in a 50Ti-47Ni-3Fe shape memory alloy during hot compressive deformation, *J. Alloys Compd.* **693** (2017) 426–431. http://dx.doi.org/10.1016/j.jallcom.2016.09.228.

[26] H. Pang, Q. Li, X. Chen, P. Chen, X. Li, J. Tan, Dynamic recrystallization mechanism and precipitation behavior of Mg-6Gd-3Y-3Sm-0.5Zr alloy during hot compression, *Met. Mater. Int.* **29** (2023) 390–401. https://doi.org/10.1007/s12540-022-01242-4.

[27] N. D. Stepanov, D. G. Shaysultanov, N. Y. Yurchenko, S. V. Zherebtsov, A. N. Ladygin, G. A. Salishchev, M. A. Tikhonovsky, High temperature deformation behavior and dynamic recrystallization in CoCrFeNiMn high entropy alloy, *Mater. Sci. Eng. A* **636** (2015) 188–195. http://dx.doi.org/10.1016/j.msea.2015.03.097.

[28] S. M. Fatemi-Varzaneh, A. Zarei-Hanzaki, H. Beladi, Dynamic recrystallization in AZ31 magnesium alloy, *Mater. Sci. Eng. A* **456** (2007) 52–57. doi:10.1016/j.msea.2006.11.095.

[29] W. Lu, W. Guo, Z. Wang, J. Li, F. An, G. Dehm, D. Raabe, C. H. Liebscher, Z. Li, Advancing strength and counteracting embrittlement by displacive transformation in heterogeneous high-entropy alloys containing sigma phase, *Acta Mater.* **246** (2023) 118717. https://doi.org/10.1016/j.actamat.2023.118717.

[30] Y. Yang, T. Chen, L. Tan, J. D. Poplawsky, K. An, Y. Wang, G. D. Samolyuk, K. Littrell, A. R. Lupini, A. Borisevich, E. P. George, Bifunctional nanoprecipitates strengthen and ductilize a medium-entropy alloy, *Nature* **595** (2021) 245–249. https://doi.org/10.1038/s41586-021-03607-y.

[31] A. Javaid, F. Czerwinski, Effect of hot rolling on microstructure and properties of the ZEK100 alloy, *J. Magnes. Alloys* **7** (2019) 27–37. https://doi.org/10.1016/j.jma.2019.02.001.

[32] J. Moon, O. Bouaziz, H. S. Kim, Y. Estrin, Twinning engineering of high-entropy alloys: An exercise in process optimization and modeling, *Mater. Sci. Eng. A* **822** (2021) 141681. https://doi.org/10.1016/j.msea.2021.141681.

[33] J. W. Bae, J. Lee, A. Zargaran, H. S. Kim, Enhanced cryogenic tensile properties with multi-stage strain hardening through partial recrystallization in a ferrous medium-entropy alloy, *Scr. Mater.* **194** (2021) 113653. https://doi.org/10.1016/j.scriptamat.2020.113653.

[34] H. T. Jeong, H. K. Park, K. Park, T. W. Na, W. J. Kim, High-temperature deformation mechanisms and processing maps of equiatomic CoCrFeMnNi high-entropy alloy, *Mater. Sci. Eng. A* **756** (2019) 528–537. https://doi.org/10.1016/j.msea.2019.04.057.

[35] R. A. Vandermeer, D. Juul Jensen, Microstructural path and temperature dependence of recrystallization in commercial aluminum, *Acta Mater.* **49** (2001) 2083–2094. https://doi.org/10.1016/S1359-6454(01)00074-X.

[36] G. Dan Sathiaraj, W. Skrotzki, A. Pukenas, R. Schaarschuch, R. Jose Immanuel, S. K. Panigrahi, J. Arout Chelvane, S. S. Satheesh Kumar, Effect of annealing on the microstructure and texture of cold rolled CrCoNi medium-entropy alloy, *Intermetallics* **101** (2018) 87–98. https://doi.org/10.1016/j.intermet.2018.07.014.

[37] A. A. Gazder, M. Sánchez-Araiza, J. J. Jonas, E. V. Pereloma, Evolution of recrystallization texture in a 0.78 wt.% Cr extra-low-carbon steel after warm and cold rolling, *Acta Mater.* **59** (2011) 4847–4865. https://doi.org/10.1016/j.actamat.2011.04.027.

[38] J. Gu, S. Ni, Y. Liu, M. Song, Regulating the strength and ductility of a cold rolled FeCrCoMnNi high-entropy alloy via annealing treatment, *Mater. Sci. Eng. A* **755** (2019) 289–294. https://doi.org/10.1016/j.msea.2019.04.025.

[39] Z. H. Fu, B. J. Yang, M. Chen, G. Q. Gou, H. Chen, Effect of recrystallization annealing treatment on the hydrogen embrittlement behavior of equimolar CoCrFeMnNi high entropy alloy, *Int. J. Hydrog.* **46** (2021) 6970–6978. https://doi.org/10.1016/j.ijhydene.2020.11.154.

[40] M. V. Klimova, D. G. Shaysultanov, S. V. Zherebtsov, N. D. Stepanov, Effect of second phase particles on mechanical properties and grain growth in a CoCrFeMnNi high entropy alloy, *Mater. Sci. Eng. A* **748** (2019) 228–235. https://doi.org/10.1016/j.msea.2019.01.112.

[41] F. Xiong, R. Fu, Y. Li, B. Xu, X. Qi, Influences of nitrogen alloying on microstructural evolution and tensile properties of CoCrFeMnNi high-entropy alloy treated by cold-rolling and subsequent annealing, *Mater. Sci. Eng. A* **787** (2020) 139472. https://doi.org/10.1016/j.msea.2020.139472.

[42] F. Otto, A. Dlouhý, Ch. Somsen, H. Bei, G. Eggeler, E. P. George, The influences of temperature and microstructure on the tensile properties of a CoCrFeMnNi high-entropy alloy, *Acta Mater.* **61** (2013) 5743–5755. https://doi.org/10.1016/j.actamat.2013.06.018.

[43] Z. Wu, X. Xu, Y. Zhao, X. Yan, Y. Zhou, L. Wei, Y. Yu, Investigation of accelerated recrystallization behavior via electropulsing treatment in CoCrFeMnNi high-entropy alloy, *Mater. Sci. Eng. A* **863** (2023) 144536. https://doi.org/10.1016/j.msea.2022.144536.

[44] S. Zhang, Y. Liu, J. Wang, S. Qin, X. Wu, F. Yuan, Tensile behaviors and strain hardening mechanisms in a high-Mn steel with heterogeneous microstructure, *Materials* **15** (2022) 3542. https://doi.org/10.3390/ma15103542.

[45] J. D. Yoo, K.-T. Park, Microband-induced plasticity in a high Mn–Al–C light steel, *Mater. Sci. Eng. A* **496** (2008) 417–424. https://doi.org/10.1016/j.msea.2008.05.042.

[46] I. Gutierrez-Urrutia, A. Shibata, K. Tsuzaki, Microstructural study of microbands in a Fe-30Mn-6.5Al-0.3C low-density steel deformed at cryogenic temperature by combined electron channeling contrast imaging and electron backscatter diffraction, *Acta Mater.* **233** (2022) 117980. https://doi.org/10.1016/j.actamat.2022.117980.

[47] M. Yang, Y. Pan, F. Yuan, Y. Zhu, X. Wu, Back stress strengthening and strain hardening in gradient structure, *Mater. Res. Lett.* **4** (2016) 145–151. https://doi.org/10.1080/21663831.2016.1153004.

[48] M. Chen, J. Li, H. Liu, M. Wang, S. Xing, Y. Zhao, Achievement of high strength-ductility combination in austenitic and ferritic duplex stainless steel by heterogeneous deformation, *J. Mater. Res. Tech.* **21** (2022) 943–950. https://doi.org/10.1016/j.jmrt.2022.09.090.

[49] M.-Y. Luo, T.-N. Lam, P.-T. Wang, N.-T. Tsou, Y.-J. Chang, R. Feng, T. Kawasaki, S. Harjo, P. K. Liaw, A.-C. Yeh, S. Y. Lee, J. Jain, E-W. Huang, Grain-size-dependent microstructure effects on cyclic deformation mechanisms in CoCrFeMnNi high-entropy-alloys, *Scr. Mater.* **210** (2022) 114459. https://doi.org/10.1016/j.scriptamat.2021.114459.

[50] C. C. Tasan, Y. Deng, K. G. Pradeep, M. J. Yao, H. Springer, D. Raabe, Composition dependence of phase stability, deformation mechanisms, and mechanical properties of the CoCrFeMnNi high-entropy alloy system, *JOM* **66** (2014) 1993–2001. https://doi.org/10.1007/s11837-014-1133-6.

[51] A. J. Zaddach, C. Niu, C. C. Koch, D. L. Irving, Mechanical properties and stacking fault energies of NiFeCrCoMn high-entropy alloy, *JOM* **65** (2013) 1780–1789. https://doi.org/10.1007/s11837-013-0771-4.

[52] G. D. Sathiaraj, M. Z. Ahmed, P. P. Bhattacharjee, Microstructure and texture of heavily cold-rolled and annealed fcc equiatomic medium to high entropy alloys, *J. Alloys Compd.* **664** (2016) 109–119. http://dx.doi.org/10.1016/j.jallcom.2015.12.172.

[53] L. Bracke, K. Verbeken, L. A. I. Kestens, Texture generation and implications in TWIP steels, *Scr. Mater.* **66** (2012) 1007–1011. http://dx.doi.org/10.1016/j.scriptamat.2012.02.048.

Graphical abstract
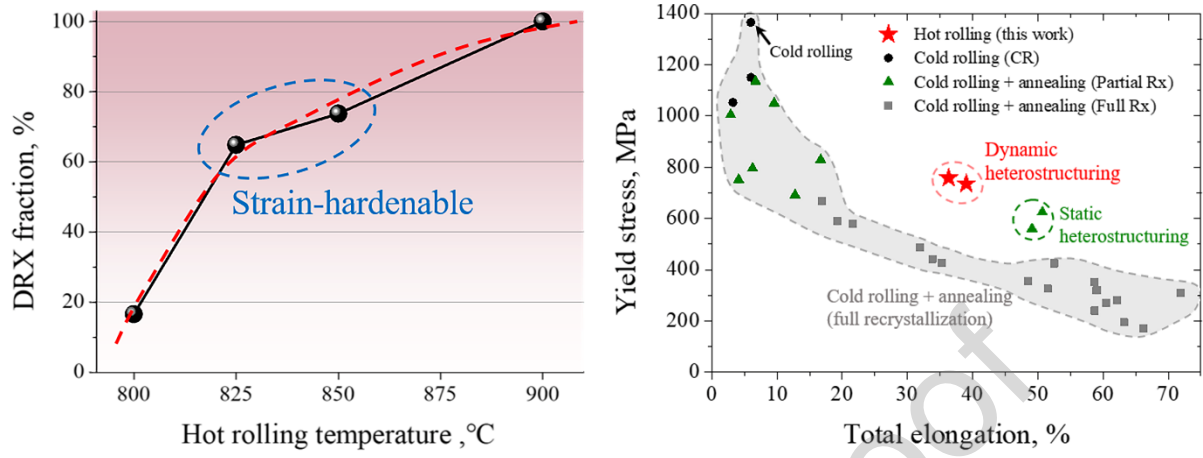
CRediT author statement

Jungwan Lee: Conceptualization, Data curation, Formal analysis, Investigation, Methodology, Validation, Visualization, Writing – Original Draft

Hyojin Park: Investigation, Methodology

Sujung Son: Investigation, Methodology

Takayoshi Nakano: Investigation

Hyoung Seop Kim: Conceptualization, Funding acquisition, Project administration, Resources, Supervision, Writing – Review & Editing

Conflict of interests

☒ The authors declare that they have no known competing financial interests or personal relationships that could have appeared to influence the work reported in this paper.

☐The authors declare the following financial interests/personal relationships which may be considered as potential competing interests:

Highlights

- Hot rolling at certain temperatures induces partial dynamic recrystallization.

- Microstructural heterogeneity of grain size and internal dislocation density rises.

- Strain incompatibility gives uniform elongation of 13% despite as-rolled states.

- A number of dislocations generated by hot rolling result in enhanced yield stress.

- This study shows more concise heterostructuring process by single-step hot rolling.